

Using dust to constrain dark matter models

Adam J. Ussing,^{1,2,3}★ Robert Adriel Mostoghiu Paun,^{1,2,3} Darren Croton,^{1,2,3} Celine Boehm,^{2,4}
 Alan Duffy,^{1,2} and Chris Power,^{3,5}

¹*Centre for Astrophysics and Supercomputing, Swinburne University of Technology, PO Box 218, Hawthorn VIC 3122, Australia*

²*ARC Centre of Excellence for Dark Matter Particle Physics (CDM)*

³*ARC Centre of Excellence for All Sky Astrophysics in 3 Dimensions (ASTRO 3D)*

⁴*School of Physics, The University of Sydney, NSW 2006, Australia*

⁵*International Centre for Radio Astronomy Research (ICRAR), M468, University of Western Australia, 35 Stirling Hwy, Crawley, WA 6009, Australia*

Accepted XXX. Received YYY; in original form ZZZ

ABSTRACT

In this paper, we use hydrodynamic zoom-in simulations of Milky Way-type haloes to explore using dust as an observational tracer to discriminate between cold and warm dark matter universes. Comparing a cold and 3.5keV warm dark matter particle model, we tune the efficiency of galaxy formation in our simulations using a variable supernova rate to create Milky Way systems with similar satellite galaxy populations while keeping all other simulation parameters the same. Cold dark matter, having more substructure, requires a higher supernova efficiency than warm dark matter to achieve the same satellite galaxy number. These different supernova efficiencies create different dust distributions around their host galaxies, which we generate by post-processing the simulation output with the `POWDERDAY` codebase. Analysing the resulting dust in each simulation, we find ~ 4.5 times more dust in our cold dark matter Milky Way halos compared with warm dark matter. The distribution of dust out to R_{200c} is then explored, revealing that the warm dark matter simulations are noticeably less concentrated than their cold dark matter counterparts, although differences in substructure complicate the comparison. Our results indicate that dust is a possible unique probe to test theories of dark matter.

Key words: dark matter – galaxies: evolution – galaxies: formation – dust, extinction – software: simulations

1 INTRODUCTION

The leading description of the cosmology of the Universe, known as Λ cold dark matter (CDM), combines a model for dark energy, Λ , with cold dark matter, some non-interacting massive particles assumed to be non-relativistic during a significant fraction of the evolution of the universe. This description has been remarkably successful in explaining various phenomena in the large-scale Universe, including the angular power spectrum of the cosmic microwave background (Aghanim et al. 2020) and baryonic acoustic oscillations (Eisenstein et al. 2005). Nevertheless, despite numerous observations supporting the existence of dark matter (Zwicky 1933; Rubin et al. 1985; Clowe et al. 2006), a dark matter particle has yet to be found, leaving its true nature as one of the great mysteries in science.

There has been a vast array of experiments designed to detect an imprint of dark matter particles, both through direct and indirect detection methods. Altogether, these experiments have probed an enormous mass range, from 10^{-22} eV up to TeV scales (see Klasen et al. (2015) for a review), though with limited sensitivity. So far, all these experiments have set stringent limits on the dark matter parameter space (mass and interaction rate with ordinary matter or a hypothetical dark sector), except for the DAMA experiment. They claimed the detection of an annual modulation signal compatible with a cold dark matter particle in the late 1990s (Bernabei et al.

2000), and maintain this claim as the DAMA/LIBRA experiment (Bernabei et al. 2008, 2021). This signal is in strong tension with the recent findings from the XenonnT (Aprile et al. 2023), LZ (Aalbers et al. 2023) and the plethora of other direct detection experiments, including those using a similar technique (Coarasa et al. 2024; Adhikari et al. 2021), which is difficult to explain theoretically. There is also a possible hint in favour of dark matter particles from the excess of gamma-rays from the galactic centre found in the FERMI-LAT data (Goodenough & Hooper 2009; Hooper & Goodenough 2011), which is also highly debated (see, e.g. Song et al. (2024) for the latest analysis). If confirmed, this would correspond to a ~ 30 GeV candidate with very suppressed interactions with nuclei to evade the direct detection limits. A dark matter discovery will take more than two highly debated hints (especially given the plethora of negative searches), so the best way to progress is to exploit the wealth of information coming from astrophysical observations. These observations are particularly useful to probe whether dark matter is collisionless (e.g. Boehm & Schaeffer 2005; Boehm et al. 2014; Mosbech et al. 2023), and if so, determine the lower bound of the particle mass (e.g. Nadler et al. 2021a). The abundance of negative direct detection searches combined with the flexibility of fits to astronomical data allows for the possibility of a more exotic dark matter particle.

The physical properties of different candidate dark matter particles manifest as macroscopic differences on astronomical scales, which are often expressed phenomenologically as cold and warm models of dark matter. To combat the difficulties in observing dark matter in the

★ E-mail: aussing@swin.edu.au

Universe, cosmological simulations have been used to quantify which characteristics of a particular dark matter model best fit the observations. Results from early cold dark matter simulations were able to shed light on several dark matter properties, such as the discovery of a universal halo density profile across a wide range of mass scales, and the abundance of intermediate to high mass haloes (Navarro et al. 1996; Springel et al. 2005). However, these early simulations also resulted in several well-known tensions with observations, for example, the missing satellites problem (Klypin et al. 1999; Moore et al. 1999), the core-cusp problem (de Blok 2010), and the too-big-to-fail problem (Boylan-Kolchin et al. 2012), see Sales et al. (2022) for a recent review. Much research has been dedicated to resolving these tensions by improving the quality of the simulations (e.g. Crain et al. 2015; Kaviraj et al. 2017; Pillepich et al. 2018; Hernández-Aguayo et al. 2022; Schaye et al. 2023). These more advanced simulations in recent years bring higher resolutions with better force accuracy and, importantly, the inclusion and advancement of baryonic models.

The missing satellites problem has been the subject of much examination. State-of-the-art Λ CDM simulations of the 1990s and early 2000s overproduced low-mass dark matter haloes by an order of magnitude compared to expectations based on Milky Way satellite observations of the time. Alternative dark matter models were seen as one possible solution, in particular, warm dark matter. Warm dark matter models introduce a free-streaming scale below which dark matter density fluctuations are erased, thus reducing the number of haloes at high redshift and eventually the number of satellites around Milky Way-like galaxies (Bode et al. 2001; Avila-Reese et al. 2001; Boehm & Schaeffer 2005). The scale at which these low-mass objects are suppressed is set by the mass of the dark matter particle. A heavier warm dark matter particle would look more similar to cold dark matter, whereas a lighter particle produces a much more significant suppression of low-mass halo formation.

The other accepted solution to the missing satellites problem generally invokes baryonic physics to suppress star formation in low mass haloes, often using the feedback of supernova (Governato et al. 2007; Sawala et al. 2016). The energy generated by a supernova event is transferred back into the gas in the simulations, heating the gas. In low-mass haloes with shallow gravitational potential wells, supernova feedback can cause gas outflows with enough energy to eject gas out of the halo entirely, eventually halting star formation. In larger haloes, supernovae still drive outflows, but the potential wells are generally deep enough to retain the gas, which can be accreted back into the galaxy. More efficient supernova models¹, where stars capable of going supernova are formed at higher rates, are able to suppress star formation in more massive galaxies, though as galaxies get larger AGN become the dominant form of feedback (Croton et al. 2006). Alternatively, reionisation was proposed as a solution to the missing satellites problem (Bullock et al. 2000; Benson et al. 2002), where the photons heat the gas to such a point that low mass haloes can't cool the gas to form galaxies. Importantly, suppression due to reionisation still allows the formation of low-mass galaxies, but preferentially for haloes that form prior to reionisation; thus, the reionisation simulation parameters can be tuned to match satellite observations.

The tensions between simulations and observations have also been eased in recent years by more complete surveys of the satellite galaxies around the Milky Way (e.g. McConnachie 2012; McConnachie

& Venn 2020). These surveys have been able to observe more low luminosity galaxies and galaxy remnants (streams). Combining the updated observations with increasingly precise modelling has led authors such as Sales et al. (2022) to conclude that the missing satellites problem can be fully explained within a cold dark matter universe.

However, baryonic solutions to the missing satellites problem come with their own complications. The feedback mechanisms used to reduce low-mass galaxy formation are often conceptually similar but numerically inconsistent between simulations. Supernova feedback alone has an array of implementations across popular codebases, including simply increasing nearby gas temperature (Springel & Hernquist 2003; Governato et al. 2007), to more complicated kinetic and thermal feedback descriptions (Dalla Vecchia & Schaye 2008; Chaikin et al. 2023). In reality, there are many forms of feedback, from AGN and supernova to photo-heating, which all come with their own implementations within different simulation codes (for a recent review see Vogelsberger et al. 2020). While simulations using a Λ CDM cosmology can solve the missing satellites problem through high efficiency feedback, the solutions are degenerate with each other and not mutually exclusive of warm dark matter. There is still work to be done to find methods to distinguish between dark matter models.

In this paper, we explore a new method for distinguishing the underlying dark matter species in simulations. It is well known that the missing satellites problem can be solved by implementing either a warm dark matter with reduced feedback efficiency or cold dark matter with increased feedback efficiency. Therefore, we combine each dark matter type with different supernova efficiencies to create simulations with similar Milky Way satellite populations. However, supernovae are also critically important in the creation and transportation of dust (Aguirre 1999; Todini & Ferrara 2001; Bianchi & Schneider 2007), and so these different supernova efficiencies are expected to produce different dust properties around the host halo. We explore if these different dust properties can then be used to infer (or at least discriminate) the underlying dark matter model. The techniques we present to analyse the dust provide a proof of concept that can be leveraged in future work with more in-depth analysis of dust in simulations and observations.

This paper is organised as follows. In Section 2, we discuss the codes used and simulation setup. Section 3 explains the simulation results with a discussion following in Section 4. We conclude in Section 5. Throughout this paper we assume a flat Planck18 cosmology (Aghanim et al. 2020), where $H_0 = 66.88$, $\Omega_m = 0.321$, $\Omega_\Lambda = 0.679$, $\Omega_b = 0.045$, $\sigma_8 = 0.840$, and $n_s = 0.9626$.

2 SIMULATIONS

2.1 Simulation code setup

For the primary analysis, we perform zoom-in hydrodynamic simulations focusing on Milky Way-like systems. We run cold and warm dark matter, the latter having a mass of 3.5 keV. This is in tension with more stringent observational constraints on the warm dark matter mass (Viel et al. 2013; Nadler et al. 2021a,b; Dekker et al. 2022), but within the limits set by Benito et al. (2020) and Newton et al. (2021). The lighter mass is used to ensure an identifiable difference in the small-scale structure that is wholly attributed to the choice of dark matter.

To generate initial conditions for each cold and warm dark matter simulation, we use music, the Multi-Scale Initial Conditions generator (Hahn & Abel 2011). We apply the Eisenstein & Hu (1998)

¹ Throughout this text, we refer to ‘supernova efficiency’ as the stellar mass fraction converted to supernova, i.e. the β parameter in Equation 1 of Springel & Hernquist (2003).

Parameter	Parent simulation	Zoom simulations
Box side length	$65h^{-1}\text{Mpc}$	$65h^{-1}\text{Mpc}$
Dark matter mass resolution	$5.68 \times 10^8 h^{-1} M_\odot$	$2.44 \times 10^6 h^{-1} M_\odot$
Baryon mass resolution	NA	$3.99 \times 10^5 h^{-1} M_\odot$
Stellar mass resolution	NA	$3.99 \times 10^5 h^{-1} M_\odot$
Force resolution	$10h^{-1}\text{kpc}$	$500h^{-1}\text{pc}$

Table 1. Summary of simulation parameters in the parent simulation (left) and the zoom-in re-simulation (right). Box side length is the comoving length of the whole simulation box; the three mass resolutions are the masses of the different particle species, and force resolution refers to the equivalent Plummer softening ϵ , and gravity becomes Newtonian at 2.8ϵ .

fitting function to create the input power spectra for the cold dark matter simulations and assume a truncated power spectrum for the warm dark matter simulations, using the [Viel et al. \(2005\)](#) transfer of the fitting function. The [Viel et al. \(2005\)](#) parameterisation of the transfer function gives us a warm dark matter half mode mass, $M_{hm} \simeq 2.3 \times 10^8 M_\odot$, at which point we expect significant divergence between cold and warm dark matter simulations. This work is focused on relative differences, so the fitting functions are accurate enough compared to traditional Boltzmann solvers. MUSIC disregards any extra thermal velocity the warm dark matter particles may carry in the initial conditions, which can produce extra spurious haloes if not treated correctly ([Klypin et al. 1993](#); [Colín et al. 2008](#)). Using this generalised approach to generate the warm dark matter power spectrum avoids any assumptions about the nature of the particle itself. The initial conditions for all simulations are created with the same random seed.

We run the parent dark matter only and the subsequent zoom-in simulations with GADGET-4 ([Springel et al. 2021](#)), an N-body and SPH code with significant improvements to older versions of GADGET. GADGET-4 makes use of a TreePM algorithm ([Xu 1995](#); [Bagla 2002](#)) for the collisionless particles and a pressure-entropy SPH prescription ([Springel & Hernquist 2002](#)) for the gas particles. The gravitational potential is softened with a cubic spline kernel and becomes Newtonian at distances $r \geq 2.8\epsilon$, where epsilon is the simulation force resolution, and the SPH properties are smoothed over 64 nearest neighbours. The baryonic prescriptions implemented with the public release of GADGET-4 are discussed in Section 2.3. Finally, we use a Friends-of-Friends algorithm ([Davis et al. 1985](#)) and SUBFIND-HBT ([Han et al. 2018](#); [Springel et al. 2021](#)) for halo and subhalo identification.

Both parent and zoom-in simulations are run from redshift $z = 127$ to $z = 0$, with a box side length of $65h^{-1}\text{Mpc}$, noting that the zoom region is $\sim 0.1\%$ the total volume. The parent simulations have 512^3 equal mass dark matter particles, which equates to an approximate mass resolution of $6 \times 10^8 h^{-1} M_\odot$ and a force resolution of $10h^{-1}\text{kpc}$. The zoom-in simulations have a dark matter particle resolution of $2.4 \times 10^6 h^{-1} M_\odot$ and a gas particle resolution of $4 \times 10^5 h^{-1} M_\odot$. More details about the simulations can be found in Table 1. The parent simulations are used to identify the haloes resembling the Milky Way halo to resimulate.

2.2 Target selection

The halo catalogues produced by SUBFIND-HBT ([Springel et al. 2021](#)) are used to identify haloes similar in mass to the Milky Way in the parent cold and warm dark matter simulations. We select haloes with a mass M_{200c} between $1\text{--}2 \times 10^{12} h^{-1} M_\odot$, where M_{200c} is the mass enclosed with a radius R_{200c} such that the density is 200 times the critical density of the universe, ρ_c . This is consistent with observed

Milky Way masses from [Bland-Hawthorn & Gerhard \(2016\)](#). We then apply an isolation criterion to these haloes. We exclude any potential resimulation target if there is another halo with a mass greater than $0.5 \times 10^{12} h^{-1} M_\odot$ within $8h^{-1}\text{Mpc}$. This ensures that the Milky Way analogue is the largest object in the resimulated region, and that we aren't investigating a galaxy undergoing a major merger. We use the same criteria and check both warm and cold dark matter parent simulations to verify the target halo exists in both simulations with similar properties. If there are multiple haloes that fit these criteria, we use the halo closest to the centre of the box.

2.3 Baryonic model

We make use of the baryonic prescriptions that come as part of the public release of GADGET-4. These include a simplified version of the [Springel & Hernquist \(2003\)](#) model for star formation and supernova, and the [Katz et al. \(1996\)](#) model for radiative cooling. The star formation model is a multi-phase model with prescriptions for the separate treatment of hot and cold gas, forming stars from cold gas after reaching a pressure threshold, and adopts a [Salpeter \(1955\)](#) initial mass function (IMF). Supernovae are assumed to happen within a single timestep in the simulation, where some fraction of the cold gas designated for star formation is immediately transferred to the hot gas phase. The cooling module treats hydrogen and helium atomic cooling in collisional equilibrium, with the abundances of the ionisation states calculated using an external ultraviolet background field, following a modified [Haardt & Madau \(1996\)](#) spectrum ([Davé et al. 1999](#)). We adopt this simple baryonic model for straightforward comparisons between our simulations. The baryonic model doesn't include stellar winds or supernova-driven outflows, which is simplistic compared to state-of-the-art models (e.g. [Crain et al. 2015](#); [Pillepich et al. 2018](#); [Davé et al. 2019](#)), but more complex models require more complex analysis beyond the scope of this analysis.

We run two simulations for each dark matter type, with different supernovae efficiency parameters, four in total. This is to determine which parameters create the most degenerate solution in the satellite populations when compared with local satellite observations. These are efficiencies of 10%, the fiducial value quoted in [Springel & Hernquist \(2003\)](#) for a Salpeter IMF, and 5%, knowing that a reduced supernovae efficiency is required in a warm dark matter simulation to produce similar numbers of low mass galaxies as a cold dark matter simulation. As highlighted in Section 1, the efficiencies here refer to the β parameter used in [Springel & Hernquist \(2003\)](#), which is the mass fraction of new stars that become supernova within one simulation timestep.

2.4 Dust production

To produce dust throughout the galaxy in our simulations, we use the post-processing tool POWDERDAY ([Narayanan et al. 2021](#)), which is built on YT ([Turk et al. 2011](#)), HYPERION ([Robitaille 2011](#)), and FSPS ([Conroy & Gunn 2010](#)). POWDERDAY is designed to provide observational properties of galaxies in cosmological simulations by assigning dust masses to the simulation gas particles according to one of several prescriptions based on observational correlations. These include a dust-to-metals ratio, a gas-to-dust ratio from [Rémy-Ruyer et al. \(2014\)](#), and a 'best-fit' metallicity dependant gas-to-dust ratio from [Li et al. \(2019\)](#).

All models are explored in this work. However, for clarity and simplicity, we focus on our results using a dust-to-metals ratio with a value of 0.4 ([Dwek 1998](#); [Yajima et al. 2015](#)). In this case, the dust

mass is calculated by multiplying the gas mass by metallicity by 0.4, where the default metal yield in `GADGET-4` is 0.02. A short comparison between dust production methods is presented in Appendix A.

2.5 Gini coefficients

The Gini coefficient is used to characterise the spatial distribution of dust produced in each simulation. Gini coefficients typically measure uniformity in a sample. When used in processes such as galaxy imaging, the scores typically represent photon flux across pixels in a CCD, where a value of 0 would mean perfect equality in the flux across all pixels, and 1 indicates all flux exists in a single pixel (Abraham et al. 2003; Lotz et al. 2004; Zamojski et al. 2007).

In our analysis, we use the Gini coefficient to describe the concentration of dust in the halo. We create a 2D projection map of the dust mass in the halo, with a bin width of $2.5h^{-1}\text{ckpc}$, and use the total mass in each bin to calculate the Gini score, G :

$$G = \frac{\sum_{i=1}^n \sum_{j=1}^n |x_i - x_j|}{2n^2\bar{x}}, \quad (1)$$

where x_n is the value in the n th cell, and \bar{x} is the average over n cells. The dust mass is calculated out to a radius of $500h^{-1}\text{ckpc}$, which equates roughly twice R_{200c} at $z = 0$; however, bins outside of R_{200c} or within a circle with a 15ckpc radius at the centre of the halo are masked to exclude them from the Gini calculation. The former avoids counting bins beyond the halo with no dust, which would lower the Gini score, and the latter avoids the highly concentrated central galaxy, which saturates any signal. To avoid projection effects, where satellites might lie directly behind or in front of the central galaxy, we rotate the dust projection maps around each axis. We use 25 viewing angles between 0 and 2π in the x - y , x - z , and y - z axes, then take the median of the 75 individual Gini score calculations. The masking is applied in every projection at all viewing angles. This method is explored further in Appendix B.

3 RESULTS

3.1 Milky Way reproduction

Before analysing the simulations, we convert their comoving units to physical units and remove the h dependence to compare with each other and later observational data. We then verify that our simulations all produce similar halo properties at $z = 0$. Each pair of dark matter simulations produces very similar Milky Way-like galaxies, with percent level differences in radius, total mass, and dark matter mass, which are summarised in Table 2. There are minor differences in the gas and stellar mass, which is to be expected from the differing supernova efficiencies. Comparing the two dark matter models against each other, we see that cold dark matter produces slightly larger haloes on average than warm dark matter, approximately 10% larger in total mass and 3% larger radii. Minor differences between the haloes are to be expected, as the different dark matter models natively produce different formation histories, and the supernova efficiencies give each galaxy a unique evolution. However, these differences between the simulations are within the expected numerical variance.

Table 2 also shows the observed values for selected Milky Way properties, taken from Bland-Hawthorn & Gerhard (2016), against which we can compare the four simulations. Our resimulation target

selection process ensures that we recover a total halo mass in the range of $1\text{--}2 \times 10^{12} M_\odot$. Our stellar masses are generally consistent, though a little larger than the observations, which tend to fall between $4\text{--}7 \times 10^{10} M_\odot$ (see also Kafle et al. 2014; Licquia & Newman 2015; McMillan 2017). Star formation rates also agree with the observations, which are between 1 to $3 M_\odot \text{yr}^{-1}$ (Chomiuk & Povich 2011; Licquia & Newman 2015; Elia et al. 2022). See Bland-Hawthorn & Gerhard (2016) for a review of the Milky Way properties.

3.2 Calibrating the simulations

The most significant point of difference between the dark matter models is the satellite galaxies, which we now compare in our simulations. We plot the cumulative satellite mass function for the Milky Way analogues in Figure 1, with the ten brightest Milky Way satellites overplotted in red triangles. We use observed satellite masses from Table 1 of Lovell & Zavala (2023) and references therein. For this work, we define a satellite galaxy in the simulation as a subhalo with at least one stellar particle and at least 100 total particles, corresponding to a minimum stellar mass of $6 \times 10^5 M_\odot$ and a minimum total mass of $6 \times 10^8 M_\odot$. The minimum total particle number limit is implemented to try to avoid artificial haloes known to plague warm dark matter simulations (Wang & White 2007; Power et al. 2016). In this setup, these artificial haloes will dominate the mass function at $M_{\text{lim}} \approx 1 \times 10^6 M_\odot$ (Wang & White 2007; Lovell et al. 2014), which is well below our halo mass resolution limit. While we include anything with a singular star particle, most satellites contain ≥ 10 star particles and generally several hundred gas and dark matter particles. Contrary to expectations, the warm dark matter simulation with 5% supernova efficiency produces the most satellite galaxies of all the simulations. We expect this is a unique case where the satellites have merged at different times rather than a trend in the simulation. We discuss this further in Section 4.2. All the simulations show good agreement with the observed number of satellites, but with so few, it's difficult to distinguish the effect of the combination of dark matter models and feedback efficiencies.

To better highlight the satellite population degeneracy between simulations, in Figure 2, we present the entire population of satellite galaxies. This figure shows a similar cumulative mass function, but now for all satellites in the box rather than only those around the Milky Way analogue. In order to be classified as a satellite in this context, the FOF group must contain no low-resolution dark matter particles. Additionally, the subhalo must contain at least one star particle and must not be rank 0, the `SUBFIND` convention for identifying the host halo. We see the expected divergence at lower masses, with both warm dark matter simulations producing fewer satellites overall than their cold dark matter counterparts. The different supernova efficiencies also show the expected behaviour, with higher rates producing fewer satellites. We find a relatively consistent match between the cold dark matter simulation with a 10% supernova efficiency rate and the warm dark matter simulation with a 5% rate. We designate these two simulations as our fiducial models for our analysis below.

3.3 Dust comparison across the simulations

After verifying that two of our models create degenerate satellite galaxy populations, both with each other and observed Milky Way satellites, we now study the dust in each simulation to determine whether it can be used as an observable to distinguish between cold and warm dark matter.

Table 3 shows the total dust mass across all simulations, within

Simulation	R_{200c} (kpc)	M_{200c} ($10^{12}M_{\odot}$)	M_{DM} ($10^{12}M_{\odot}$)	M_{gas} ($10^{10}M_{\odot}$)	M_{stars} ($10^{10}M_{\odot}$)	SFR ($M_{\odot}yr^{-1}$)
CDM - SN 5%	261.8	1.9	1.6	12.9	12.0	2.5
CDM - SN 10%	261.6	1.9	1.6	13.8	10.8	1.6
WDM - SN 5%	254.1	1.7	1.5	11.0	11.6	1.4
WDM - SN 10%	254.0	1.7	1.5	11.1	11.4	1.6
Milky Way	169-284	0.55-2.62	-	1-5	4-7	1-3

Table 2. Summary halo information for the Milky Way analogue in each simulation. All units are physical with h factored in. M_{200c} refers to the total mass within the radius R_{200c} , M_{DM} , M_{gas} , and M_{stars} refer to the dark matter, gas, and stellar masses, respectively, within the same halo radius. SFR is the star formation rate within the Milky Way analogue. Ranges for the observed Milky Way values are taken from [Bland-Hawthorn & Gerhard \(2016\)](#).

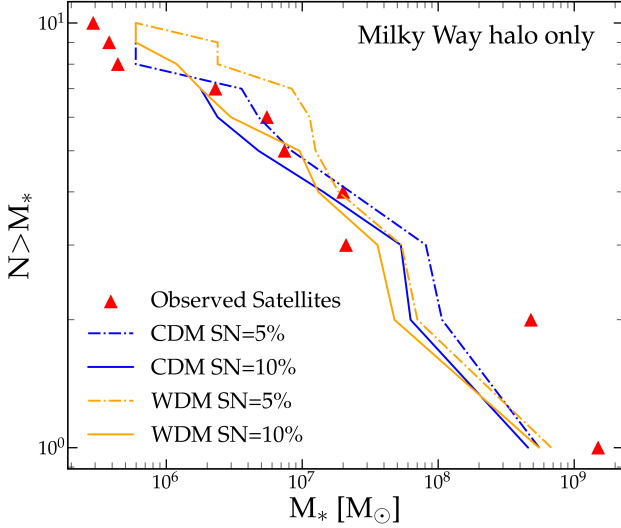


Figure 1. The cumulative satellite galaxy population around each Milky Way analogue in our warm and cold dark matter simulations, with two levels of supernova efficiencies. Blue lines indicate cold dark matter, and orange for warm dark matter; dash-dot lines indicate 5% supernova efficiency and solid lines 10%. The red triangles mark the ten largest observed Milky Way satellites; their masses are taken from the compilation by [Lovell & Zavala \(2023\)](#).

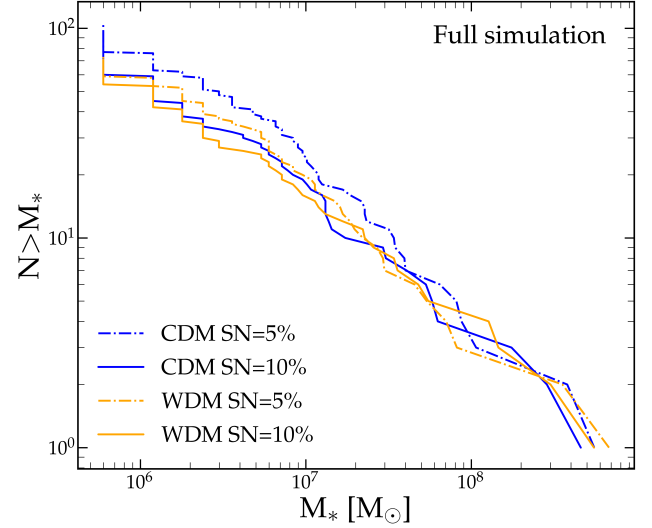


Figure 2. The complete cumulative satellite galaxy population (not just the Milky Way analogue) within each simulation box. We see general convergence between the models in the high-mass satellites, and a divergence between the different dark matter models at the low-mass end, where the impact of supernovae efficiency also becomes more evident. The most degenerate solutions are a cold dark matter simulation with 10% supernova and warm dark matter with 5%.

Simulation	Dust Mass R_{200c} ($10^7 M_{\odot}$)	Dust Mass 15kpc ($10^7 M_{\odot}$)	Dust Mass 15kpc (%)
CDM - SN 5%	1.44	1.22	85%
CDM - SN 10%	4.56	3.98	87%
WDM - SN 5%	1.05	0.79	75%
WDM - SN 10%	2.52	2.36	93%

Table 3. The total dust mass produced in our four simulations (see Table 1), measured both within the halo radius and the inner 15kpc around the central Milky Way analogue galaxy. The majority of the dust is concentrated within the central galaxy of the halo.

R_{200c} and the central 15kpc, using the dust-to-metals prescription described in Section 2.4. Crucially, the difference between the fiducial cold (10%) and warm (5%) dark matter models (the two best matching configurations) is significant, with > 4 times the total amount of dust in the cold dark matter simulation. An increase in supernovae efficiency increases the amount of dust in both dark matter models, though less so for warm dark matter. The lower supernova efficiency effectively locks away more gas in stars, reducing the availability of gas for star-forming episodes that drive increases in metallicity. The concentration, or the fraction of dust within 15kpc of the halo centre, ranges from 75% in the fiducial warm dark matter simulation to up

to 87% in the fiducial cold dark matter simulation. This presents the possibility that direct observations of the dust inside a galaxy can be used as a metric to differentiate the nature of the dark matter species, in terms of aggregated dust masses.

To explore dust outside of the galaxy (but inside the halo), Figures 3a and 3b plot the 2D projections of its distribution out to the halo radius for our fiducial cold and warm dark matter simulations. Beyond the central galaxy, the remaining dust tends to be concentrated in the satellites, with lower densities in the diffuse gas. The differential map between the two simulations is shown in Figure 3c. The colour bar shows the percentage difference between the two, with blue indicating higher dust mass in the cold dark matter simulation and red indicating higher dust mass in the warm dark matter simulation. This comparison shows the same behaviour as that of the total mass, that generally, there is more dust in the cold dark matter simulation spread throughout the halo. Besides this general interpretation, the differential map has several key features. The most obvious is that the difference in satellite positions creates stark differences in the differential dust map, even if their positions are only marginally offset. The other interesting feature is the difference in dust distribution around the central galaxy. The cold dark matter simulation has a much more compact dust disk than the warm dark matter simulation, which is primarily driven by the difference in supernova efficiencies. When

we switch the efficiencies, i.e. cold dark matter with a 5% supernova efficiency and warm dark matter with a 10% efficiency, we see the opposite trend, where the cold dark matter has a much more extended dust disk. This switch doesn't significantly affect the dust outside of the central galaxy.

To better understand the difference in dust mass between the simulations, we plot the dust surface density as a function of the radius at $z = 0$ in Figure 4. We over-plot the scaling relation $\Sigma_{\text{dust}} \propto r^{-0.8}$ from Ménard et al. (2010) with a scaling amplitude $\lambda=0.03$ for the dust-to-metals ratio, chosen to match the densities of the simulations at radii $\gtrsim 15\text{kpc}$, as well as a red arrow the point where gravity becomes Newtonian, and a dashed line at the masking radius. We also plot the radial dust surface density of M31, the closest Milky Way analogue to the Milky Way Galaxy. The surface density is taken from Draine et al. (2014), where they find a total estimated dust mass of $5.4 \times 10^7 M_{\odot}$. Our results generally agree with the M31 observations in amplitude and shape at intermediate radii, between 10-20kpc, although inner regions have higher densities than M31. The high-density central regions are potentially inflated by limitations of our baryonic model; future refinements could add stellar winds or AGN feedback to help drive gas into the circumgalactic medium and lower the dust content in the central galaxy. The cold dark matter simulation with 10% supernova efficiency is additionally inflated by a recent close pass by a merging satellite, which happens at larger radii for the other cold dark matter simulation and not at all in the warm dark matter simulations. All simulations follow the Ménard et al. (2010) scaling relation at radii greater than $\gtrsim 20\text{kpc}$ with little deviation. Outside of the central galaxy, all simulations have similar surface density profiles.

Appendix A shows the comparison between all dust mass prescriptions introduced in Section 2.4, where we find similar results and interpretations.

3.4 Gini results

In Section 2.5, we introduced the Gini score, which we now apply to our projected dust surface maps to further discriminate between their distributions and how this changes with time. The Gini score allows us to condense the information in maps like those in Figures 3a and 3b, into a single number. This is calculated for all halo rotations (see Section 2.5) between $z = 1.22$ and $z = 0$, and is plotted in the top panel of Figure 5. The shaded regions in the plot show 1σ bootstrap errors for the medians at each redshift. The relative difference in Gini score with respect to the 10% cold dark matter simulation is shown in the bottom panel of Figure 5, with the same errors as above.

At higher redshift, cold and warm dark matter simulations share similar Gini scores and evolutions, but this begins to diverge around $z = 0.5$. Both warm dark matter simulations have lower concentrations of dust and hence a lower score than both cold dark matter simulations, and the gap between them grows with time. Supernova feedback efficiency doesn't appear to significantly impact the Gini score for a given dark matter type. The stochastic nature of the overall score is primarily governed by the merger history; for a universe such as warm dark matter with fewer low mass haloes and fewer merger events, we expect reduced Gini scores compared to a purely cold dark matter universe. This is a promising result as a proof of concept. Future work will focus on a wider range of Milky Way-like haloes and galaxy histories to explore the significance of the variance of such statistics.

4 DISCUSSION

There are several aspects of our results and analysis that require further discussion. In this section, we explore the main differences in our results between simulations, issues around measuring the Milky Way satellite population when drawing our conclusions, the impact of our choice of dust model in our hydrodynamic simulations, and finally, a discussion of the Gini statistic and how it is used in our analysis to draw conclusions.

4.1 Simulations

Our simulations and subsequent dust post-processing show that we have potentially uncovered a new observational probe to test the nature of dark matter. Through the use of varying supernova efficiencies as our lever, we created simulations from different underlying dark matter types that produce the same “observable” satellite populations. These different supernova efficiencies lead to different dust properties in each halo. We find that the total dust mass produced by the fiducial cold dark matter simulation, with a 10% supernova efficiency, is ~ 4 times greater than in the fiducial warm dark matter simulation. We also presented a preliminary exploration of how dust is spatially distributed within the halo using the Gini statistic, which shows significant and persistent differences between dark matter models. The difference between the two suggests that dust can be used as an observational probe of the underlying dark matter. In reality, galactic dust masses are influenced by many factors, such as star formation histories (Calzetti et al. 2000; Clemens et al. 2013), mergers (Buck et al. 2023), and environments (Chelouche et al. 2007; Vogelsberger et al. 2019; Clark et al. 2023), so more work must be done before we draw conclusions about any observationally favoured model.

4.2 Milky Way satellites

There are many different sources for the mass of Milky Way satellites, which introduces some uncertainty into the correct values against which to calibrate the simulations. We use the masses published in Lovell & Zavala (2023) for all satellites included in the comparison in Figure 1. This maintains a single source of data for simplicity and transparency, but does not explore the uncertainty of masses for these satellites. Many stellar masses are taken from McConnachie (2012), which has minor differences with other published masses for these satellites (Woo et al. 2008; Fattahi et al. 2018), though all are quite consistent for the larger satellites. Additionally, there is some scatter in the dynamical masses compared with Strigari et al. (2008) and Wolf et al. (2010), but once again, being the largest Milky Way satellites, the scatter in these measurements is relatively small.

Counterintuitively, Figure 1 shows that the fiducial warm dark matter simulation produces more low-mass satellite galaxies than any other simulation, as mentioned in Section 3.2. This is rather unexpected, given that warm dark matter is generally implemented to decrease satellite numbers. The apparent overproduction in the simulation² could be due to a number of factors, first among them the artificial fragmentation common in warm dark matter simulations (Wang & White 2007). We have explored removing such artificial halos by implementing a minimum 100-particle limit. Our testing suggests that artificial halos are not the cause of the excess. More

² Although we note that both warm dark matter simulations produce fewer *total subhaloes* than their cold dark matter counterparts.

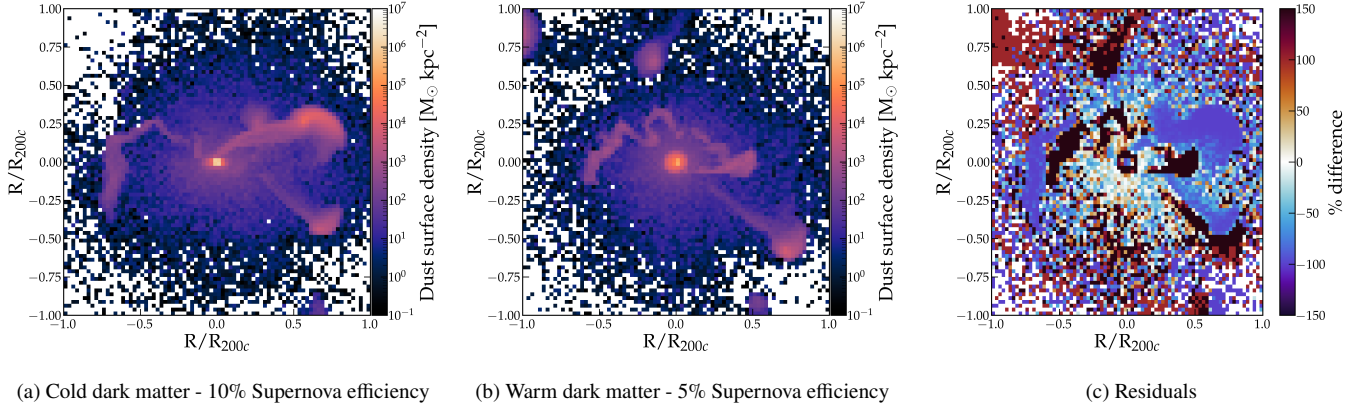


Figure 3. *Left & Middle:* Dust map projection plots around our Milky Way analogue galaxies, showing cold dark matter with a 10% supernovae efficiency on the left, and warm dark matter with 5% supernovae efficiency in the middle. The projection extends out to R_{200c} . *Right:* The percentage difference of the dust mass between the two simulations. High values in red show more dust in the warm dark matter simulation and low values in blue show more dust in cold dark matter.

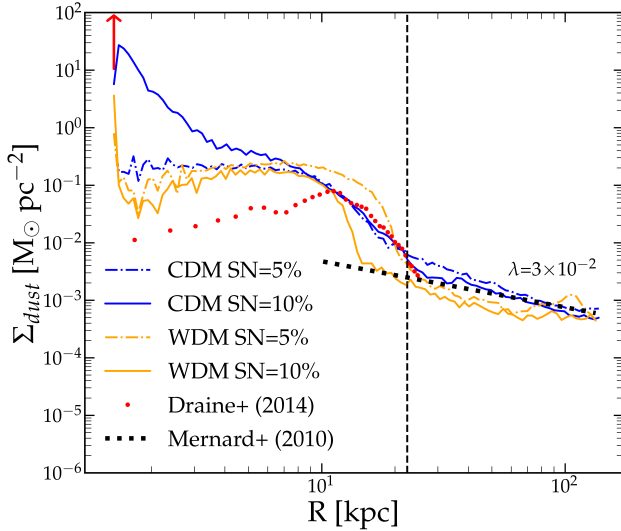


Figure 4. The dust surface density as a function of radius for all our simulations, at $z = 0$. The grey dotted line is the scaling relation described in Ménard et al. (2010), with an amplitude of 0.03, chosen to match the simulations at radii $\geq 15 \text{ kpc}$. The red points show the dust surface density from observations of M31 from Draine et al. (2014). The vertical dashed line shows the masking radius of $15 h^{-1} \text{ kpc}$, and the red arrow shows the point at which gravitational forces become Newtonian.

work is needed to identify spurious haloes, e.g. identifying pancake haloes in the initial conditions (Lovell et al. 2014), but this is beyond the scope of this paper. Alternatively, Oman et al. (2024) found that warm dark matter may boost the number of low-mass galaxies in 21-cm hydrogen observations. They state this may be because galaxies tend to form later in warm dark matter simulations, and the subsequent delay in star formation helps them retain more gas than their cold dark matter counterparts. Additionally, the higher concentration of cold dark matter haloes may drive faster merging times, causing an excess of warm dark matter satellites that have yet to fully merge by the same point in time. This may be true, at least for our Milky Way analogue. We defer such an investigation to later work, conscious that the most stringent limits on warm dark matter particle masses are based on the observation of satellites below

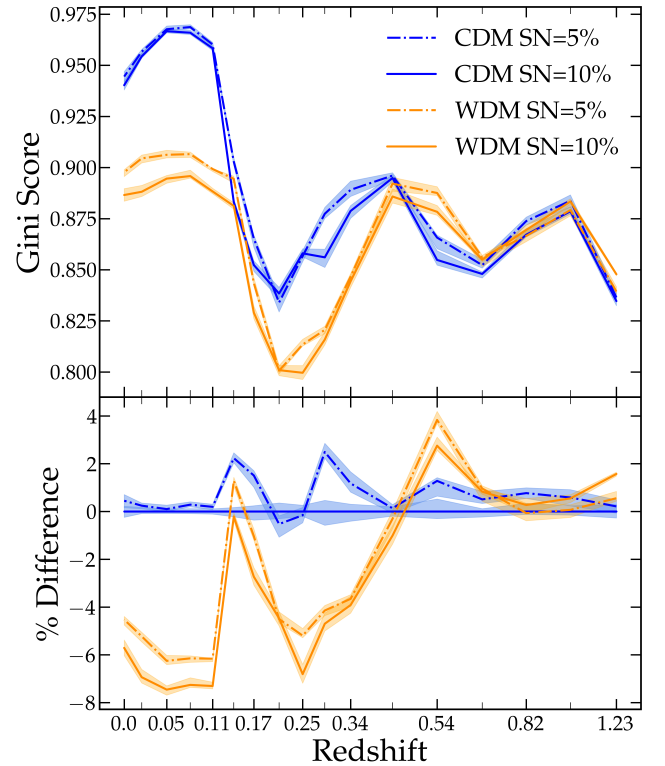


Figure 5. *Top:* The Gini scores calculated from the dust distributions within the halo (e.g. Figure 3), where we mask the galaxy with a radius of $15 h^{-1} \text{ kpc}$, across all simulations from $z = 1.22$ to $z = 0$. The scores are calculated from a series of projections and then averaged for each snapshot. The shaded regions show 1σ errors from a bootstrap resample of the 75 projections; the blue regions show errors for each cold dark matter simulation, and the orange regions for each warm dark matter simulation. *Bottom:* The percentage differences between the Gini scores, normalised by the 10% cold dark matter simulation. Errors are the same as above.

the resolution of these simulations (Banik et al. 2021; Nadler et al. 2021a; Dekker et al. 2022). However, the possibility of a warm dark matter universe potentially producing more satellite galaxies in some haloes prompts further investigation into the variety of pathways for

satellite accretion in a warm dark matter universe and how these might compare with our own Milky Way satellites.

4.3 Dust

As the goal of this paper is to provide a simple proof of concept, we chose the simplest `POWDERDAY` model to generate dust from our hydrodynamic simulations, the dust-to-metals ratio. This correlation has a long track record in the literature (Silva et al. 1998; James et al. 2002; Lacey et al. 2008; Somerville et al. 2012; Yajima et al. 2015; Ma et al. 2019). While there are more detailed implementations of dust scaling relations and more advanced subgrid models that treat dust evolution (e.g. McKinnon et al. 2016; Aoyama et al. 2018), we make this choice to keep the comparisons between simulations and the observations straightforward and transparent. However, we tested two other dust mass prescriptions included in `Powderday` to confirm the results from the dust-to-metals ratio.

These two models were the Rémy-Ruyer et al. (2014) gas-to-dust ratio and the Li et al. (2019) best-fit set of parameters. In short, the dust-to-metals ratio produces the least total dust in all simulations, and the best-fit model produces the most dust in all simulations. All prescriptions produce highly concentrated dust distributions, though the transition in the gas-to-dust and best-fit prescriptions is more extreme from high to low densities. Despite these differences in the spatial distribution between dust mass prescriptions, we have confirmed they don't significantly change the Gini scores. Further comparison of the dust models is provided in Appendix A.

4.4 Gini Trends

The difference in the Gini evolution produced by our simulations is an encouraging sign that the dust around a galaxy contains spatial information that can be used to differentiate between dark matter models. The individual Gini scores appear to be governed more strongly by the halo evolution rather than the baryonic model, which has two primary implications. Firstly, the diffuse dust is more dependent on the amount of substructure than the baryonic model. This is impacted by masking the central galaxy, where most of the dust is concentrated. For example, the gas disk is much more extended in the 5% warm dark matter simulation in Figure 3b compared to the 10% cold dark matter simulation in Figure 3a. By masking this region to avoid saturating the Gini signal, we are also masking the region with the greatest difference caused by our implemented baryonic model.

The second implication is that every halo in our simulation has a unique evolution, even when starting from the same initial conditions and random seed. This unique evolution makes direct extrapolation of a Gini score to the observations difficult. However, the relative difference in the simulations highlights a difference that can be leveraged in observations. The absolute values for the total dust mass and Gini scores will likely change as a function of the random initial seed. Still, we expect that a warm dark matter universe, with fewer average mergers, will produce lower Gini scores over a large sample. Any prediction for an average Gini score in dust observations would require many simulations and careful treatment of the comparison between the two; though not beyond the capabilities of modern telescopes, with JWST and ALMA observations able to achieve sub-kpc resolution at $z \approx 1$ (e.g. Liu et al. 2024). This is beyond the scope of the current work but will be the focus of our future work.

We see modest changes in the absolute Gini score across all prescriptions, but little change in the shape of the evolution. This is explored further in Appendix A.

5 CONCLUSIONS

We have tested a novel method for distinguishing between cold and warm dark matter using the dust around a galaxy. We ran zoom-in simulations of Milky Way analogues, tuning the efficiency of the supernova feedback to create systems with degenerate satellite galaxy populations. The different supernova efficiencies create different dust populations, which are used as the observational probe between dark matter models.

Our simulations take identical random seeds to create the initial conditions. The parent dark matter only simulations are then used to identify Milky Way analogues, hosted by haloes with a mass of approximately $2 \times 10^{12} M_{\odot}$. Once identified, we ensure the haloes are isolated, to make sure there isn't another large halo within 8 Mpc. After identifying target haloes in both the cold and warm dark matter parent simulations, the zoom-in simulations were run with 5% and 10% supernova efficiencies. The resimulated Milky Way analogue galaxies all show general agreement with observed quantities of the real Milky Way (see Table 2).

We post-processed each simulation using `POWDERDAY` (Narayanan et al. 2021) to produce the dust properties, based on the simulated gas particle properties. The results presented here use a dust-to-metals ratio of 0.4 (Dwek 1998; Yajima et al. 2015), and we confirmed they are not overly sensitive to the precise dust prescription. `POWDERDAY` produces distinct dust properties for each simulation, from which the main results from the dust analysis are as follows.

(i) The different supernova efficiencies produce different dust masses; the fiducial cold dark matter simulation produces the most at $4.56 \times 10^7 M_{\odot}$, compared to $1.05 \times 10^7 M_{\odot}$ in the fiducial warm dark matter simulation. All dust masses are listed in Table 3.

(ii) The majority of the dust is always contained within the inner 15kpc of the halo, evident in Figure 3. We see a generally higher dust mass with cold dark matter across much of the halo (Figure 3c). There are regions with obvious differences, which are largely generated by differences in satellite positioning and an extended galactic disk in the warm dark matter simulation.

(iii) The dust surface density profiles seen in Figure 4 show good agreement with the Ménard et al. (2010) scaling relation, $\Sigma_{\text{dust}} \propto r^{-0.8}$, at radii larger than $\sim 20\text{kpc}$. Between 10 to 20kpc, most simulations match reasonably well with the Draine et al. (2014) dust observations of M31, though, below these scales, the fiducial cold dark matter simulation has a rising density profile, whereas both warm dark matter simulations and the 5% cold dark matter simulation have flat density profiles.

(iv) We calculated the Gini coefficient of each dust distribution, masking the inner 15kpc to study the diffuse dust, in Figure 5. We compared the evolution of the dust concentration across all four simulations, finding that a warm dark matter universe produces lower concentrations of dust. The evolution of the dust concentration is impacted more so by the merger history than the supernova efficiency, indicating these sorts of spatial studies can be leveraged by observations of dust around Milky Way-type galaxies.

Our results show that cold and warm dark matter simulations can produce similar satellite galaxy populations with different dust distributions. The total dust mass is different across all simulations, and there is a clear separation in the evolution of the masked Gini scores for these galaxies. There are two clear avenues for future work. The first is to use more advanced baryonic models, potentially with self-consistent dust treatment. As previously mentioned in Section 2.3, the baryonic models used are simplistic compared to current flagship simulations. However, using more complex models requires more

effort to disentangle the effects of the subgrid routines from the different dark matter models. A more straightforward approach is to first increase the sample of galaxies used in the Gini analysis in an effort to overcome the expected variation from different random seeds. We can then compare the results with observational catalogues such as DustPedia (Davies et al. 2017) using simulated images generated by POWDERDAY. The results from this and future work pave the way for developing a new tool for determining the nature of dark matter in our Universe.

ACKNOWLEDGEMENTS

The authors would like to thank the referee, Mark Lovell, for their valuable comments in improving this publication, as well as useful discussions with Alexander Knebe and Desika Narayanan. AU and RM also acknowledge UWA/ICRAR for supporting a research visit. This research was supported in part by the Australian Government through the Australian Research Council Centre of Excellence for Dark Matter Particle Physics (CDM, CE200100008), and in part by the Australian Research Council Centre of Excellence for All Sky Astrophysics in 3 Dimensions (ASTRO 3D, CE170100013). AU acknowledges the support of an Australian Government Research Training Program Scholarship, and DC acknowledges the support of an ARC Future Fellowship (FT220100841). This work was performed on the OzSTAR national facility at Swinburne University of Technology. The OzSTAR program receives funding in part from the Astronomy National Collaborative Research Infrastructure Strategy (NCRIS) allocation provided by the Australian Government, and from the Victorian Higher Education State Investment Fund (VHE-SIF) provided by the Victorian Government.

DATA AVAILABILITY

The simulations used in this study are available and accessible on reasonable request. The data products of this work can be shared upon request to the corresponding author.

REFERENCES

Aalbers J., et al., 2023, *Physical Review Letters*, 131, 041002
 Abraham R. G., van den Bergh S., Nair P., 2003, *The Astrophysical Journal*, 588, 218
 Adhikari G., et al., 2021, *Science Advances*, 7, eabk2699
 Aghanim N., et al., 2020, *Astronomy and Astrophysics*, 641, A6
 Aguirre A., 1999, *The Astrophysical Journal*, 525, 583
 Aoyama S., Hou K.-C., Hirashita H., Nagamine K., Shimizu I., 2018, *Monthly Notices of the Royal Astronomical Society*, 478, 4905
 Aprile E., et al., 2023, *Physical Review Letters*, 131, 041003
 Avila-Reese V., Colín P., Valenzuela O., D’Onghia E., Firmani C., 2001, *The Astrophysical Journal*, 559, 516
 Bagla J. S., 2002, *Journal of Astrophysics and Astronomy*, 23, 185
 Banik N., Bovy J., Bertone G., Erkal D., de Boer T. J. L., 2021, *Journal of Cosmology and Astroparticle Physics*, 2021, 043
 Benito M., Criado J. C., Hütsi G., Raidal M., Veermäe H., 2020, *Physical Review D*, 101, 103023
 Benson A. J., Frenk C. S., Lacey C. G., Baugh C. M., Cole S., 2002, *Monthly Notices of the Royal Astronomical Society*, 333, 177
 Bernabei R., et al., 2000, *Physics Letters B*, 480, 23
 Bernabei R., et al., 2008, *European Physical Journal C*, 56, 333
 Bernabei R., et al., 2021, The dark matter: DAMA/LIBRA and its perspectives, <http://arxiv.org/abs/2110.04734>

Bianchi S., Schneider R., 2007, *Monthly Notices of the Royal Astronomical Society*, 378, 973
 Bland-Hawthorn J., Gerhard O., 2016, *Annual Review of Astronomy and Astrophysics*, 54, 529
 Bode P., Ostriker J. P., Turok N., 2001, *The Astrophysical Journal*, 556, 93
 Boehm C., Schaeffer R., 2005, *Astronomy and Astrophysics*, 438, 419
 Boehm C., Schewtschenko J. A., Wilkinson R. J., Baugh C. M., Pascoli S., 2014, *Monthly Notices of the Royal Astronomical Society*, 445, L31
 Boylan-Kolchin M., Bullock J. S., Kaplinghat M., 2012, *Monthly Notices of the Royal Astronomical Society*, 422, 1203
 Buck T., Obreja A., Ratcliffe B., Lu Y., Minchev I., Macciò A. V., 2023, *Monthly Notices of the Royal Astronomical Society*, 523, 1565
 Bullock J. S., Kravtsov A. V., Weinberg D. H., 2000, *The Astrophysical Journal*, 539, 517
 Calzetti D., Armus L., Bohlin R. C., Kinney A. L., Koornneef J., Storchi-Bergmann T., 2000, *The Astrophysical Journal*, 533, 682
 Chaikin E., Schaye J., Schaller M., Benítez-Llambay A., Nobels F. S. J., Ploekinger S., 2023, *Monthly Notices of the Royal Astronomical Society*, 523, 3709
 Chelouche D., Koester B. P., Bowen D. V., 2007, *The Astrophysical Journal*, 671, L97
 Chomiuk L., Povich M. S., 2011, *The Astronomical Journal*, 142, 197
 Clark C. J. R., Roman-Duval J. C., Gordon K. D., Bot C., Smith M. W. L., Hagen L. M. Z., 2023, *The Astrophysical Journal*, 946, 42
 Clemens M. S., et al., 2013, *Monthly Notices of the Royal Astronomical Society*, 433, 695
 Clowe D., Bradač M., Gonzalez A. H., Markevitch M., Randall S. W., Jones C., Zaritsky D., 2006, *The Astrophysical Journal*, 648, L109
 Coarasa I., et al., 2024, ANAIS-112 three years data: a sensitive model independent negative test of the DAMA/LIBRA dark matter signal, [doi:10.48550/arXiv.2404.17348](https://doi.org/10.48550/arXiv.2404.17348), <https://ui.adsabs.harvard.edu/abs/2024arXiv240417348C>
 Colín P., Valenzuela O., Avila-Reese V., 2008, *The Astrophysical Journal*, 673, 203
 Conroy C., Gunn J. E., 2010, *The Astrophysical Journal*, 712, 833
 Crain R. A., et al., 2015, *Monthly Notices of the Royal Astronomical Society*, 450, 1937
 Croton D. J., et al., 2006, *Monthly Notices of the Royal Astronomical Society*, 365, 11
 Dalla Vecchia C., Schaye J., 2008, *Monthly Notices of the Royal Astronomical Society*, 387, 1431
 Davies J. I., et al., 2017, *Publications of the Astronomical Society of the Pacific*, 129, 044102
 Davis M., Efsthathiou G., Frenk C. S., White S. D. M., 1985, *The Astrophysical Journal*, 292, 371
 Davé R., Hernquist L., Katz N., Weinberg D. H., 1999, *The Astrophysical Journal*, 511, 521
 Davé R., Anglés-Alcázar D., Narayanan D., Li Q., Rafieferantsoa M. H., Appleby S., 2019, *Monthly Notices of the Royal Astronomical Society*, 486, 2827
 Dekker A., Ando S., Correa C. A., Ng K. C. Y., 2022, *Physical Review D*, 106, 123026
 Draine B. T., et al., 2014, *The Astrophysical Journal*, 780, 172
 Dwek E., 1998, *The Astrophysical Journal*, 501, 643
 Eisenstein D. J., Hu W., 1998, *The Astrophysical Journal*, 496, 605
 Eisenstein D. J., et al., 2005, *The Astrophysical Journal*, 633, 560
 Elia D., et al., 2022, *The Astrophysical Journal*, 941, 162
 Fattahi A., Navarro J. F., Frenk C. S., Oman K. A., Sawala T., Schaller M., 2018, *Monthly Notices of the Royal Astronomical Society*, 476, 3816
 Goodenough L., Hooper D., 2009, Possible Evidence For Dark Matter Annihilation In The Inner Milky Way From The Fermi Gamma Ray Space Telescope, [doi:10.48550/arXiv.0910.2998](https://doi.org/10.48550/arXiv.0910.2998), <https://ui.adsabs.harvard.edu/abs/2009arXiv0910.2998G>
 Governato F., Willman B., Mayer L., Brooks A., Stinson G., Valenzuela O., Wadsley J., Quinn T., 2007, *Monthly Notices of the Royal Astronomical Society*, 374, 1479
 Haardt F., Madau P., 1996, *The Astrophysical Journal*, 461, 20
 Hahn O., Abel T., 2011, *Monthly Notices of the Royal Astronomical Society*,

- 415, 2101
- Han J., Cole S., Frenk C. S., Benitez-Llambay A., Helly J., 2018, *Monthly Notices of the Royal Astronomical Society*, 474, 604
- Hernández-Aguayo C., et al., 2022, The MillenniumTNG Project: High-precision predictions for matter clustering and halo statistics, doi:10.48550/arXiv.2210.10059, <http://arxiv.org/abs/2210.10059>
- Hooper D., Goodenough L., 2011, *Physics Letters B*, 697, 412
- James A., Dunne L., Eales S., Edmunds M. G., 2002, *Monthly Notices of the Royal Astronomical Society*, 335, 753
- Kaffe P. R., Sharma S., Lewis G. F., Bland-Hawthorn J., 2014, *The Astrophysical Journal*, 794, 59
- Katz N., Weinberg D. H., Hernquist L., 1996, *The Astrophysical Journal Supplement Series*, 105, 19
- Kaviraj S., et al., 2017, *Monthly Notices of the Royal Astronomical Society*, 467, 4739
- Klasen M., Pohl M., Sigl G., 2015, *Progress in Particle and Nuclear Physics*, 85, 1
- Klypin A., Holtzman J., Primack J., Regos E., 1993, *The Astrophysical Journal*, 416, 1
- Klypin A. A., Kravtsov A. V., Valenzuela O., Prada F., 1999, *The Astrophysical Journal*, 522, 82
- Lacey C. G., Baugh C. M., Frenk C. S., Silva L., Granato G. L., Bressan A., 2008, *Monthly Notices of the Royal Astronomical Society*, 385, 1155
- Li Q., Narayanan D., Davé R., 2019, *Monthly Notices of the Royal Astronomical Society*, 490, 1425
- Licquia T. C., Newman J. A., 2015, *The Astrophysical Journal*, 806, 96
- Liu Z., et al., 2024, *The Astrophysical Journal*, 968, 15
- Lotz J. M., Primack J., Madau P., 2004, *The Astronomical Journal*, 128, 163
- Lovell M. R., Zavala J., 2023, *Monthly Notices of the Royal Astronomical Society*, 520, 1567
- Lovell M. R., Frenk C. S., Eke V. R., Jenkins A., Gao L., Theuns T., 2014, *Monthly Notices of the Royal Astronomical Society*, 439, 300
- Ma X., et al., 2019, *Monthly Notices of the Royal Astronomical Society*, 487, 1844
- McConnachie A. W., 2012, *The Astronomical Journal*, 144, 4
- McConnachie A. W., Venn K. A., 2020, *Research Notes of the American Astronomical Society*, 4, 229
- McKinnon R., Torrey P., Vogelsberger M., 2016, *Monthly Notices of the Royal Astronomical Society*, 457, 3775
- McMillan P. J., 2017, *Monthly Notices of the Royal Astronomical Society*, 465, 76
- Moore B., Ghigna S., Governato F., Lake G., Quinn T., Stadel J., Tozzi P., 1999, *The Astrophysical Journal*, 524, L19
- Mosbech M. R., Boehm C., Wong Y. Y., 2023, *Journal of Cosmology and Astroparticle Physics*, 2023, 047
- Ménard B., Scranton R., Fukugita M., Richards G., 2010, *Monthly Notices of the Royal Astronomical Society*, 405, 1025
- Nadler E. O., et al., 2021a, *Physical Review Letters*, 126, 091101
- Nadler E. O., Birrer S., Gilman D., Wechsler R. H., Du X., Benson A., Nierenberg A. M., Treu T., 2021b, *The Astrophysical Journal*, 917, 7
- Narayanan D., et al., 2021, *The Astrophysical Journal Supplement Series*, 252, 12
- Navarro J. F., Frenk C. S., White S. D. M., 1996, *The Astrophysical Journal*, 462, 563
- Newton O., et al., 2021, *Journal of Cosmology and Astroparticle Physics*, 2021, 062
- Oman K. A., Frenk C. S., Crain R. A., Lovell M. R., Pfeffer J., 2024, *Monthly Notices of the Royal Astronomical Society*, 533, 67
- Pillepich A., et al., 2018, *Monthly Notices of the Royal Astronomical Society*, 473, 4077
- Power C., Robotham A. S. G., Obreschkow D., Hobbs A., Lewis G. F., 2016, *Monthly Notices of the Royal Astronomical Society*, 462, 474
- Robitaille T. P., 2011, *Astronomy and Astrophysics*, 536, A79
- Rubin V. C., Burstein D., Ford Jr. W. K., Thonnard N., 1985, *The Astrophysical Journal*, 289, 81
- Rémy-Ruyer A., et al., 2014, *Astronomy and Astrophysics*, 563, A31
- Sales L. V., Wetzel A., Fattahi A., 2022, *Nature Astronomy*, 6, 897
- Salpeter E. E., 1955, *The Astrophysical Journal*, 121, 161
- Sawala T., et al., 2016, *Monthly Notices of the Royal Astronomical Society*, 457, 1931
- Schaye J., et al., 2023, *Monthly Notices of the Royal Astronomical Society*
- Silva L., Granato G. L., Bressan A., Danese L., 1998, *The Astrophysical Journal*, 509, 103
- Somerville R. S., Gilmore R. C., Primack J. R., Domínguez A., 2012, *Monthly Notices of the Royal Astronomical Society*, 423, 1992
- Song D., et al., 2024, *Monthly Notices of the Royal Astronomical Society*, 530, 4395
- Springel V., Hernquist L., 2002, *Monthly Notices of the Royal Astronomical Society*, 333, 649
- Springel V., Hernquist L., 2003, *Monthly Notices of the Royal Astronomical Society*, 339, 289
- Springel V., et al., 2005, *Nature*, 435, 629
- Springel V., Pakmor R., Zier O., Reinecke M., 2021, *Monthly Notices of the Royal Astronomical Society*, 506, 2871
- Strigari L. E., Bullock J. S., Kaplinghat M., Simon J. D., Geha M., Willman B., Walker M. G., 2008, *Nature*, 454, 1096
- Todini P., Ferrara A., 2001, *Monthly Notices of the Royal Astronomical Society*, 325, 726
- Turk M. J., Smith B. D., Oishi J. S., Skory S., Skillman S. W., Abel T., Norman M. L., 2011, *The Astrophysical Journal Supplement Series*, 192, 9
- Viel M., Lesgourgues J., Haehnelt M. G., Matarrese S., Riotto A., 2005, *Physical Review D*, 71, 063534
- Viel M., Becker G. D., Bolton J. S., Haehnelt M. G., 2013, *Physical Review D*, 88, 043502
- Vogelsberger M., McKinnon R., O’Neil S., Marinacci F., Torrey P., Kannan R., 2019, *Monthly Notices of the Royal Astronomical Society*, 487, 4870
- Vogelsberger M., Marinacci F., Torrey P., Puchwein E., 2020, *Nature Reviews Physics*, 2, 42
- Wang J., White S. D. M., 2007, *Monthly Notices of the Royal Astronomical Society*, 380, 93
- Wolf J., Martínez G. D., Bullock J. S., Kaplinghat M., Geha M., Muñoz R. R., Simon J. D., Avedo F. F., 2010, *Monthly Notices of the Royal Astronomical Society*, 406, 1220
- Woo J., Courteau S., Dekel A., 2008, *Monthly Notices of the Royal Astronomical Society*, 390, 1453
- Xu G., 1995, *The Astrophysical Journal Supplement Series*, 98, 355
- Yajima H., Shlosman I., Romano-Díaz E., Nagamine K., 2015, *Monthly Notices of the Royal Astronomical Society*, 451, 418
- Zamojski M. A., et al., 2007, *The Astrophysical Journal Supplement Series*, 172, 468
- Zwicky F., 1933, *Helvetica Physica Acta*, 6, 110
- de Blok W. J. G., 2010, *Advances in Astronomy*, 2010, 789293

APPENDIX A: DIFFERENT DUST PRODUCTION RESULTS

The different dust mass prescriptions available in POWDERDAY are discussed here, though we note they don’t impact the results of our analysis. In addition to the dust-to-metals method presented in Section 2.4, we also ran the metallicity-dependant gas-to-dust ratio described in Rémy-Ruyer et al. (2014), as well as the best-fit combined gas-to-dust and dust-to-metals ratios from the machine learning model described in Li et al. (2019). This best-fit model produces the most dust for each simulation out of any of the tested prescriptions, while the dust-to-metals ratio produces the least. For the cold dark matter simulation with 10% supernova efficiency, the best-fit model produced a total dust mass of $29.2 \times 10^7 M_\odot$, the gas-to-dust ratio a total mass of $11.2 \times 10^7 M_\odot$, compared with $4.6 \times 10^7 M_\odot$ for the dust-to-metals method.

We show the surface density profiles for all dust prescriptions in Figure A1. These all have similar shapes, though slightly different amplitudes. The best-fit surface density profile, Figure A1c, has the

greatest peak amplitude in the centre of the halo but has the lowest surface density at larger radii. All dust mass prescriptions follow the Ménard et al. (2010) scaling at radii $\gtrsim 15$ kpc, though the dust-to-metals method produces comparatively higher masses in low density environments and so is fit better with a higher amplitude scaling.

More extreme changes in surface density are also evident in the Gini comparisons shown in Figure A2. The dust-to-metals method has the smoothest transition from the inner to outer halo in surface density (Figure A1a) and the least concentrated Gini evolution (Figure A2a). Conversely, the best-fit model has a more extreme transition in its density profile (Figure A1c) and a more concentrated Gini evolution (Figure A2c). The gas-to-dust dust mass calculation method is quite similar to the best-fit model with slightly lower concentrations of dust. Despite the differences in total dust mass and surface density profiles, the difference between warm and cold dark is persistent in all models, confirming our results above.

APPENDIX B: HALO MASKING

Here, we show the masking method used to calculate the Gini score outlined in Section 2.5. After creating the 2D projected histograms of dust mass similar to Figure 3, we take the centre of each bin, and if the centre of the bin is less than 15 kpc from the centre of the halo, the bin is excluded from the calculation. Bins are also excluded if the bin centre is beyond R_{200c} . The inner 15 kpc and R_{200} limits are in comoving units for the evolution analysis. Figure B1 shows these masked 2D projections of the halo, with the masked regions in dark green. The same masking is applied to all rotations we use to calculate the median Gini score and errors.

This paper has been typeset from a \LaTeX file prepared by the author.

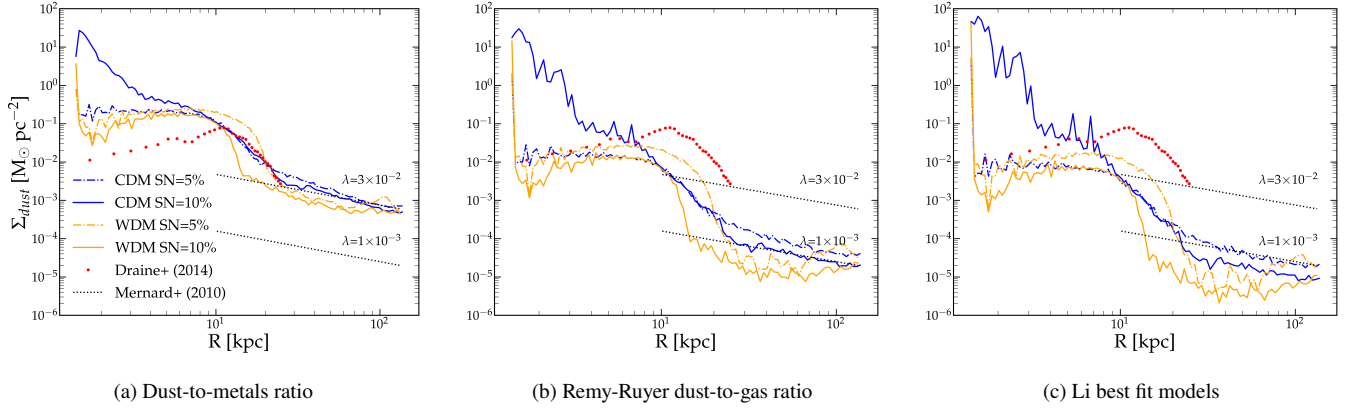


Figure A1. Comparison of the dust surface density for each dust production model from `POWDERDAY`, plus two different amplitudes for the [Ménard et al. \(2010\)](#) scaling relations, one to match the dust-to-metals ratio and the other to match both the [Rémy-Ruyer et al. \(2014\)](#) and [Li et al. \(2019\)](#) models.

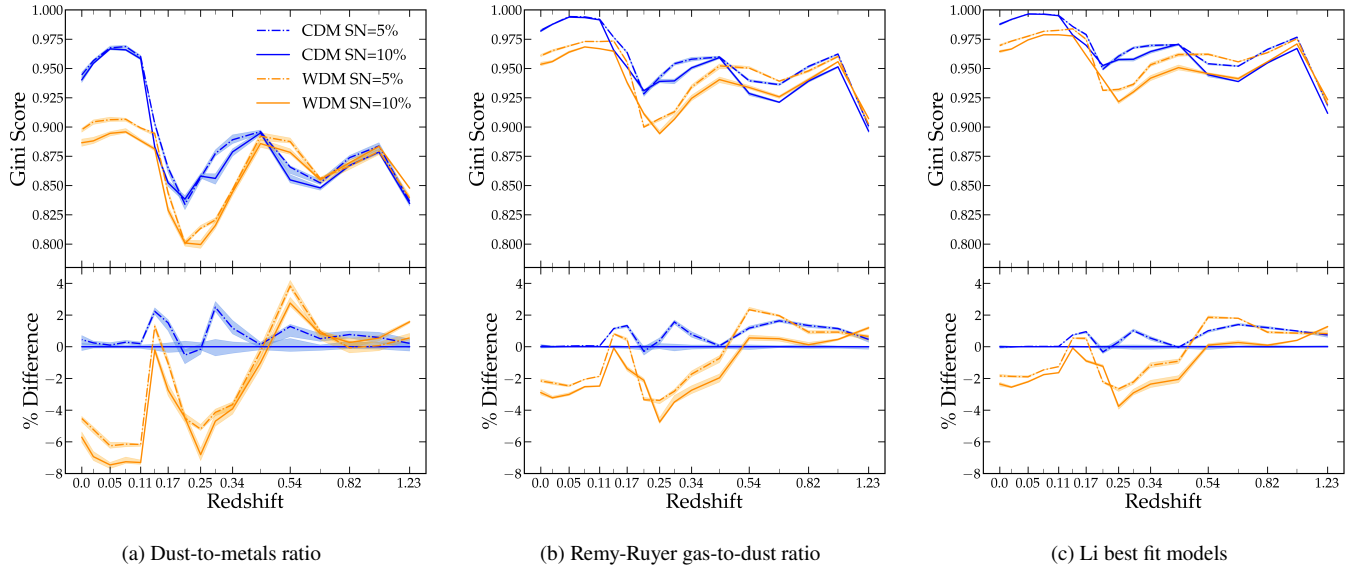


Figure A2. The Gini scores (top) and percentage differences (bottom) for each dust production model from `POWDERDAY`, plotted as a function of redshift. The amplitude of the scores differ, becoming more concentrated (higher scores) from left to right. Note, though, that the shape of the evolutions remains constant.

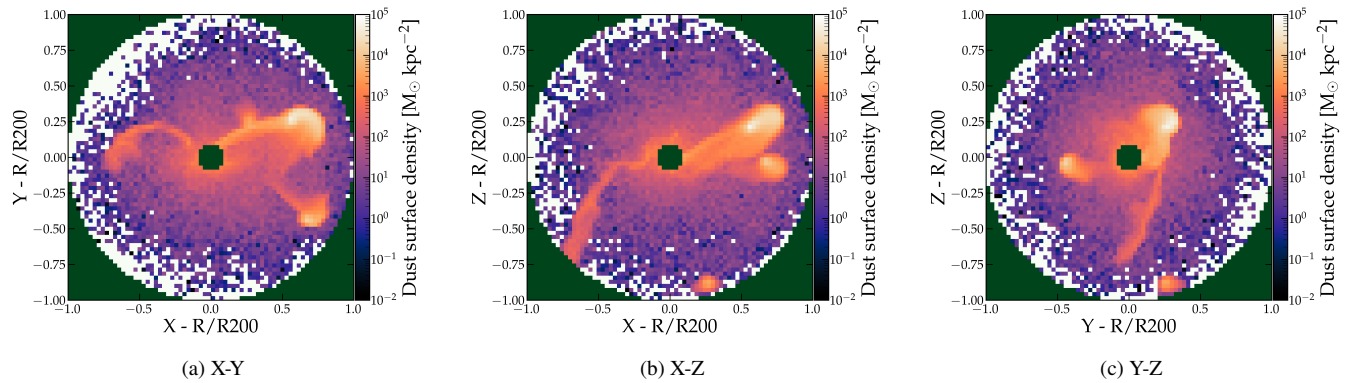


Figure B1. The masking method used for the Gini calculations. Masked bins are shown in dark green, and white bins are empty. We masked everything outside of R_{200c} , as well as the bins with a centre within 15kpc, which would otherwise saturate any signal.